Dynamic recrystallization during hot compression of Ni-based superalloy Haynes 282

N.B. When citing this work, cite the original published paper.

(article starts on next page)

Research Article

Dynamic recrystallization during hot compression of Ni-based superalloy Haynes 282

Emil Eriksson [a], Fabian Hanning [b], Joel Andersson [b], Magnus Hörnqvist Colliander [a],*

[a] *Chalmers University of Technology, 412 96 Göteborg, Sweden*
[b] *University West, Gustava Melins gata 2, 461 32 Trollhättan, Sweden*

ARTICLE INFO

ABSTRACT

Understanding the microstructural behaviour of materials during thermomechanical processing is a vital step towards optimizing the mechanical properties. One important aspect during forming processes, such as forging, is dynamic recrystallization (DRX), which sets the starting microstructure for the subsequent manufacturing steps. Here we investigated the DRX behaviour of Ni-base superalloy Haynes 282 during hot compression with a strain rate of 0.05 s^{-1} at 1080 °C, with care taken to minimize the effects of meta-dynamic recrystallization (mDRX) and adiabatic heating. Small DRX grains could be observed already at ε = 0.1, i.e. before the peak strain ε_p = 0.15. The DRX process accelerated significantly above ε = 0.2, and the material was fully recrystallized at ε = 1.5. Up to ε = 0.8 DRX occurred through continuous nucleation of new grains, whereas above ε = 0.8 the number density of DRX grains decreased and the increase in recrystallized fraction was due to growth of existing grains. Contrary to common assumptions of DRX nuclei being essentially dislocation free, many of the DRX grains contained pronounced dislocation substructures, even at small strains where they are not expected to have undergone deformation.

1. Introduction

The mechanical properties of metallic materials are controlled by their microstructure, e.g. grain size and shape, texture, and presence of secondary particles [1]. While the final properties of a component is typically determined by subsequent heat treatments, the starting microstructure originating from the prior manufacturing routes (comprising of vacuum induction melting, vacuum arc remelting and electro-slag remelting followed by forming and shaping operations) defines the available property space. Therefore, understanding the microstructural evolution during different manufacturing steps is critical for property optimization and development of new materials. This is especially important for high-performance materials such as Ni-base superalloys, which are used in demanding applications such as hot sections of aircraft engines and turbine generators [2,3]. In this article, we investigate the dynamic recrystallization (DRX) during hot compression of Ni-base superalloy Haynes 282, a new $\gamma^{'}$ strengthened alloy which shows promise as an easily fabricable and weldable alloy due to its slow $\gamma^{'}$ precipitation kinetics [4]. It consists of a face centered cubic (fcc) matrix, γ, with the main strengthening precipitate being $\gamma^{'}$ (L1$_2$ structured Ni$_3$(Ti,Al)), and secondary M$_{23}$C$_6$ and M$_6$C carbides located at grain boundaries [4,5].

While microstructure-property relationships, stability of the microstructure, and the effects of heat treatments performed after hot forming in Haynes 282 has received considerable attention [6–9], the investigations of DRX during high temperature processing are limited. Shi et al. [10] studied the hot deformation behaviour at temperatures ranges between 950 and 1210 °C, with strain rates ranging from 0.01 to 10 s^{-1}, and derived processing maps with the conclusion that optimal deformation ranges were between 1100 and 1180 °C and 0.01–0.1 s^{-1}.

We have previously investigated the dynamic and meta-dynamic (mDRX) recrystallization of Haynes 282 during hot compression at different strain rates both above and below the grain boundary carbide solvus (1100 °C) [11]. We concluded that both temperature and strain rate have an effect on the DRX process, but after a 90 s post deformation hold mDRX had erased the effect of the strain rate and the final microstructure was mainly controlled by the temperature. Similarly, Metzler et al. [12] investigated the microstructural evolution with annealing time for up to 2 h after deformation, and showed that strain rate and total strain only weakly influenced the final average grain size. In a dedicated study we also noted that M$_{23}$C$_6$ grain boundary carbides do not have a significant contribution on the recrystallization behaviour, and

---

* Corresponding author.
E-mail address: magnus.colliander@chalmers.se (M. Hörnqvist Colliander).

concluded that the carbide solvus temperature (1100 °C) is not a critical temperature in regards to DRX behaviour [13].

Gardner et al. [14] conducted single and multi-pass compression tests on Haynes 282 at 1100 °C and strain rate of 0.2 s^{-1}. They found that multi-pass tests resulted in microstructures with larger average grain size but with higher spread, as well as observing lower intragranular misorientations in multi-pass specimens.

The above studies did not, however, capture the onset and progression of DRX during compression, as they all focused on the microstructure obtained after relatively high strains (0.7–1). The early stages of DRX is still not well characterized or understood. It is often assumed to occur at the strain corresponding to the maximum stress (peak strain, ϵ_p) [15] or at the inflection point in the 2nd derivative of the work hardening rate, i.e. the point where the work hardening rate starts to decrease [16]. Contradictory to these approaches, dedicated microscopy studies of Ni-based superalloy Inconel 718 showed only very limited DRX even at strains up to $2\epsilon_p$ [17]. The determination of DRX from the macroscopic stress–strain curves is complicated by the the large variations in temperature, strain and strain rate throughout the sample volume, even for small samples [18], which prevents a unique correlation between local microstructure evolution and global mechanical response. Even in the absence of such uncertainties, the correlation between flow softening and DRX evolution is ambiguous, as the recrystallized grains will undergo deformation and the steady-state stress is correlated to a dynamic balance between nucleation and deformation. Even more direct methods, such as microscopy investigations of interrupted hot compression tests, suffer from the same problems with inhomogenous deformation and temperature fields, but also from mDRX occurring during the post-deformation quench delay [17]. In addition, discrepancies between reports could be related to the method of heating, as resistive (Joule) heating have been shown to accelerate the DRX process compared to conventional radiation furnaces [19]. It is therefore important to be careful when comparing results between studies.

We investigate the progression of DRX in Haynes 282 during hot compression. Samples have been deformed to strain levels below, at and above ϵ_p at 1080 °C and a low strain rate, 0.05 s^{-1} (in order to minimize the contribution from adiabatic heating), and quenched with minimum delay to avoid mDRX. We observe nucleated DRX grains even at the lowest strain, i.e. below ϵ_p, but at very low fractions. With increasing strain, clear substructures of low angle grain boundaries (LAGB) were observed in the deformed grains with more recrystallized grains nucleating at random high angle grain boundaries (HAGB), creating the necklace structure associated with discontinuous DRX (dDRX). The DRX process accelerated significantly at strains above 0.2, which explains the flow softening of the material. We also observe pronounced dislocation substructures in small DRX grains even at low strains, which suggests that nucleation does not necessarily involve the formation of deformation free grains.

2. Experimental procedure

Eight cylindrical samples, with length 12 mm and diameter 8 mm, for Gleeble testing were machined from a 6 in. diameter Haynes 282 billet, the composition of which is shown in Table 1. In order to have the same initial microstructure, all samples were

Table 1
Chemical composition of Haynes 282 (in wt%) according to material certificate.

Ni	Cr	Co	Mo	Ti	Al	Fe	Mn	Si	C	B
bal	19.3	10.2	8.7	2.2	1.5	0.9	0.05	< 0.05	0.06	0.004

machined at half radius distance from the centre of the billet. During industrial forging the large billets would be soaked at the forging temperature prior to deformation in order to ensure homogeneous temperature. As the deformation temperature in this study, 1080 °C, is below the carbide solvus (1100 °C [20]), the soaking would lead to precipitation of grain boundary carbides. Although the effect of such carbides are negligible [13], we chose to mimic the industrial process by subjecting all samples, including the reference sample for investigation of the initial structure, to a 30 min soak at 1080 °C in a pre-heated furnace in an atmospheric environment, followed by water quenching. Water quenching completely suppresses nucleation of γ' in Haynes 282, as was shown by Joseph et al. [21] in a dedicated atom probe tomography study.

The soaked samples were then placed in a Gleeble 3800 where the compression tests were performed. The test procedure is described in more detailed in reference [11], but is summarized here. The temperature was monitored and controlled using a thermocouple spot welded to the center of the gauge length and each sample was heated to 1080 °C over 60 s. After reaching the target temperature the samples were held for 10 s in order to stabilize the heating system and the temperature. Prior investigations with several thermo-couples along the gauge length have shown that 10 s is enough time to stabilize the temperature gradient along the gauge length. The rapid heating and hold above the γ' solvus temperature (1000 °C [20]) should prevent any significant presence of γ' in the microstructure.

The samples were deformed to different strains at a constant nominal strain rate of 0.05 s^{-1}. In order to preserve the microstructure in the state corresponding to the end of the deformation, the samples were water quenched directly after deformation. However, as shown by Nicolaÿ et al, [17], the quench delay could result in a significant contribution of changes in the microstructure via mDRX. To minimize this impact, the water nozzle was placed as close to the sample as possible while also pre-filling the hose with water. This brought the quench delay down to 0.2 s

The samples were cut along the gauge length with a low speed saw, and the cross-sections were ground using SiC papers, polished with diamond particles and lastly oxide polished in order to achieve a mirror-like surface for the electron backscattered diffraction (EBSD) investigation, which was performed in a GAIA Tescan focused ion beam-scanning electron microscope (FIB-SEM). It should be noted that the maps shown in Fig. 3, due to their size and step size of 0.5 μm, were acquired in two different runs (one of the upper and one of the lower portion) which were stitched together using HKL CHANNEL 5 map stitching tool. EBSD analysis was performed using MTex software [22]. In order to determine the types of carbides present at the grain boundaries, energy dispersive X-ray spectroscopy (EDS), performed in a JEOL Prime FEG-SEM with an acceleration voltage of 5 kV, was used.

3. Results and Discussion

3.1. Initial structure

The large (2.5 × 2.5 mm^2, step size 7 μm), inverse pole figure (IPF) map from the initial soaked billet in Fig. 1(a) shows a relatively uniform microstructure with respect to grain size, with an average grain diameter of around 107 μm, including Σ3 twins, and no preferred texture. Fig. 1(b) shows the presence and morphology of carbides. Primary MC carbides, rich in Ti [23], are large and blocky and are seen both intra- and intergranuary. Mo-rich M_6C carbides [23] appear as white particles mainly seen within grains, but also at grain boundaries, and Cr-rich $M_{23}C_6$ carbides [23] are exclusively
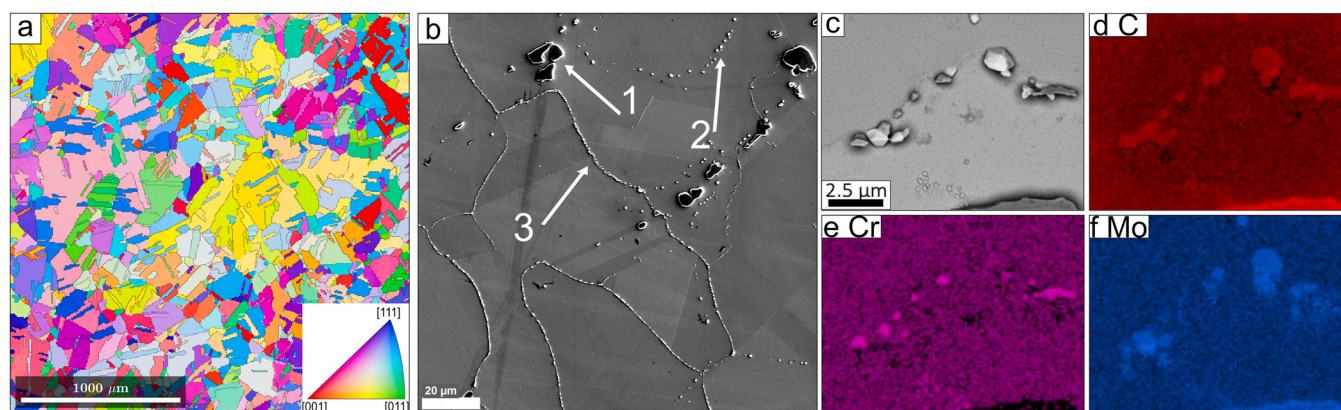
Fig. 1. Initial billet structure. (a) 2.5 × 2.5 mm² IPF with corresponding legend parallel to a horizontal axis. (b) Secondary electron (SE) image where MC (1), M_6C (2) and $M_{23}C_6$ (3) carbides are seen in the microstructure, based on the analysis performed by Joseph et al. [23]. (c–f) show EDS data from a small region containing grain boundary carbides. (c) is the SE image, while (d–f) show elemental maps for C, Cr and Mo respectively. Scale bar for these figures is 2.5 μm.
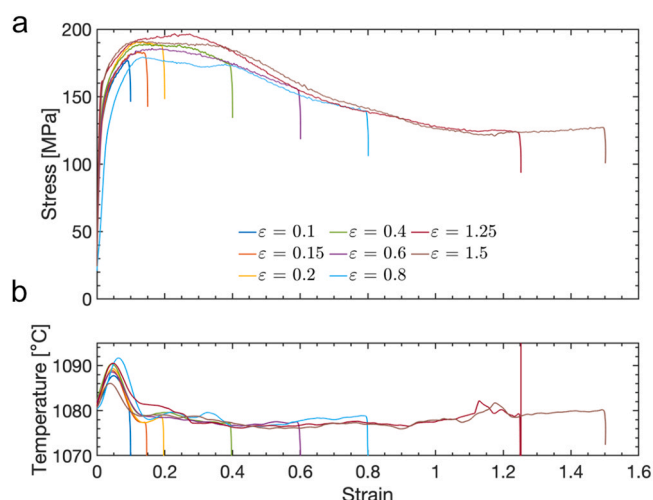
Fig. 2. Evolution of (a) true stress and (b) temperature with true strain for the different samples.

found along grain boundaries. EDS measurements of grain boundary carbides, shown in Fig. 1(c–f), was used to confirm the correlation between image contrast and morphology and carbide chemistry.

3.2. Deformation response

The stress–strain curves are shown in Fig. 2(a). Note that the "true" values are calculated based on the standard assumption of homogeneous deformation, which is violated as a result of axial temperature gradients and frictional effects [11], and should only be considered as qualitative. During the initial stages of deformation the material work hardens due to an increase in dislocation density. Eventually, the hardening rate decreases and ε_p is reached, after which flow softening is observed. The strain levels were chosen so the microstructure slightly before ($\varepsilon = 0.1$), at ($\varepsilon = 0.15$), slightly after ($\varepsilon = 0.2$) the peak strain, during the flow softening ($\varepsilon = 0.4$, 0.6 and 0.8) and in the steady state regime ($\varepsilon = 1.25$ and 1.5).

Even though a slow strain rate (0.05 s^{-1}) was chosen to minimize adiabatic heating, Fig. 2(b) shows that the temperature conditions

during compression are not isothermal. There is an initial temperature rise at the start of deformation, leading to a temperature some 10 °C above the target at $\varepsilon \approx 0.05$. Estimation of adiabatic heating suggests that the expected temperature increase is in the order of 1 °C, indicating the significantly larger increase observed here has other origins. A potential cause can be an increase in current when force is applied which led to better electrical contact between sample and anvils. After a peak the temperature at $\varepsilon \approx 0.05$ decreases to within 3–4 °C of target at $\varepsilon \approx 0.1 - 0.15$ and remains there throughout the compression. Non-isothermal response in the early stages clearly poses a problem for detailed investigations of the onset of DRX, as this is the strain region where DRX is expected to initiate. Another important aspect is the implications of the initial temperature variation on attempts to determine the early stage DRX characteristics from analyses of the stress–strain response. Many studies use the response at $\varepsilon \leq \varepsilon_p$ to calibrate a constitutive model for the "DRX-free" response as part of subsequent separation of recovery effects (saturation) and flow softening (DRX) [24,25]. The current results indicate that such calibrations could suffer from relatively large uncertainties in temperature, i.e. thermal activation, which would result in erroneous predictions of the saturation stress. Similarly, attempts to determine inflection points in the work hardening rate become problematic due to the superimposed change in temperature affecting the balance between hardening and softening thus possibly shifting the minimum. Details of the temperature response during hot compression tests are seldom reported, but this indicates that it may have critical effects on the conclusions and should be carefully considered in any analysis.

3.3. Deformed microstructure

Stitched IPF maps (500 × 500 μm², step size 0.5 μm) from the initial billet microstructure as well as from the central region of samples deformed to different strains are shown in Fig. 3. After a strain of 0.1 (Fig. 3(b)), local rotations of the lattice can mainly be seen at triple junctions. A small region of potentially recrystallized grains is visible and highlighted with a circle. The presence of DRX grains was confirmed by EBSD maps with higher magnification and resolution, see Figure S1 in the supplementary material. At strains of 0.15 (Fig. 3(c)) and 0.2 (Fig. 3(d)), corresponding to the microstructure at and just after ε_p, respectively, recrystallized grains are more clearly seen at grain boundaries in some regions, and larger
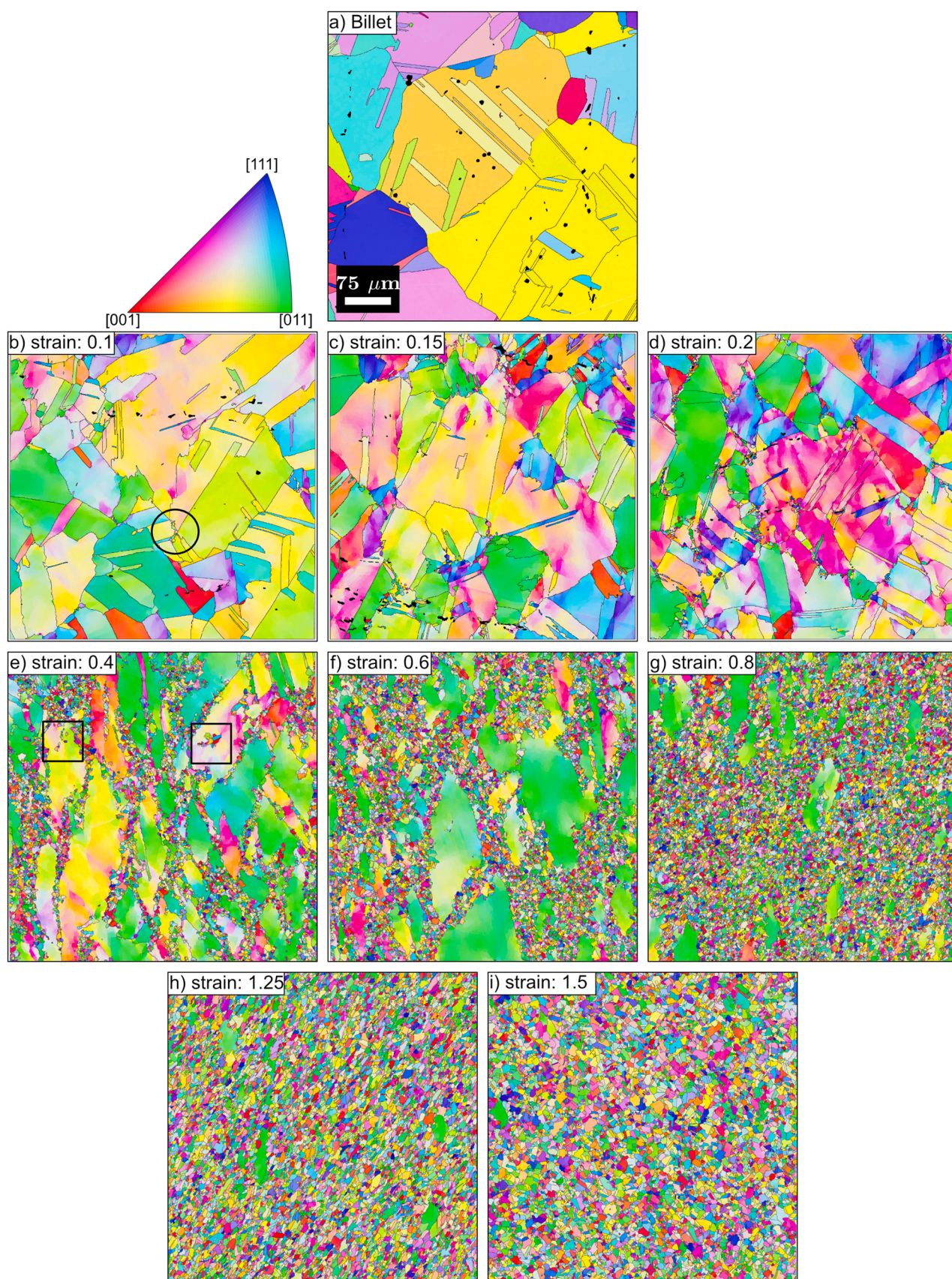
Fig. 3. Stitched IPF maps for (a) billet microstructure, and after deformation to strains of (b) 0.1, (c) 0.15, (d) 0.2, (e) 0.4, (f) 0.6, (g) 0.8 (h) 1.25 and (i) 1.5. Each map is 500 × 500 μm^2.

orientation gradients can be seen in the interior of the deformed grains, and not only at triple junctions. Due to the similarity in crystal structure between fcc Ni and MC carbides, the latter were frequently indexed as Ni. As a size-dependent threshold will be used to separate recrystallized and deformed grains (further details in section 3.4) the small MC carbides will be classified as recrystallized. This can cause significant errors when evaluating the DRX fraction at low strains ($\varepsilon \leq 0.2$), where the number of recrystallized grains is small. Therefore, the MC carbides were manually excluded by overlaying the IPF map and the SE image (where carbides were easily distinguished) and the respective grains were removed from the data set. More details on the procedure is provided in the supplementary material. They have also been marked in black in Fig. 3(a–d) to avoid confusion. However, for the larger strains, where the recrystallization is much more prominent, eventual MC carbides were left in the list of recrystallized grains as the statistical error would be negligible for these samples.

A significantly larger amount of recrystallized grains can be seen at $\varepsilon = 0.4$ (Fig. 3(e)), which suggests that the rate of recrystallization accelerates at strains above 0.2. Here, recrystallized grains are observed at practically all grain boundaries, even between what is most likely Σ3 boundaries, where no recrystallization was visible at lower strains. Given their low energy, [26], Σ3 boundaries are not expected to be preferential sites for recrystallization. Miura et al. [27] showed that triple junctions where at least one boundary was a Σ3 twin were less likely to act as recrystallization sites. Recrystallization also occurs locally inside grains, see e.g. regions indicated by black squares in Fig. 3(e). This is most likely the cause of particle stimulated nucleation (PSN), where MC carbides (located either above or below the investigated surface) act as nucleation sites [11]. Continued compression results in an even higher fraction of recrystallized grains at grain boundaries, creating the so called necklace structure commonly associated with dDRX. At a strain of 0.8 (Fig. 3(e)) the microstructure is still not fully recrystallized, consistent with our previous observations under the same conditions [11]. While remains of deformed grains are clearly seen at $\varepsilon = 1.25$ (Fig. 3(g)), the microstructure is in principle fully recrystallization at a strain of 1.5 and the grains have undergone visible growth (Fig. 3(h)).

3.4. DRX kinetics

In order to measure the evolution of the DRX fraction, X_{DRX}, grains were classified as *recrystallized* or *deformed*, based on a grain size (equivalent diameter) threshold set to 10 μm. The use of a size threshold, rather than e.g. grain orientation spread (GOS) was chosen as it gave a more robust differentiation in the current microstructures with a large size difference between deformed and recrystallized grains [28]. Fig. 4 shows the same maps as in Fig. 3 but with recrystallized grains in red and deformed in grey. As mentioned, for strains 0.1, 0.15 and 0.2, where the amount of recrystallized grains was small, the MC carbides were manually removed prior to analysis. Another artefact present at low strains was a number of small regions within deformed twins were classified as recrystallized, although from their Σ3 boundaries they were evidently twinned regions extending perpendicular to the cross-section. They were much fewer than the amount of MC carbides, but they were also removed from the DRX grains, instead shown as deformed in Fig. 4. Due to the very small number of recrystallized grains and the manual corrections applied, the relative uncertainty in the DRX fraction at the smallest strains is large, but as the fraction

is low (although certainly greater than zero, as discussed in the preceding section) this uncertainty does not have a significant impact on the following analysis. At the highest strain levels ($\varepsilon \geq 0.6$), on the other hand, there is a risk that remnants of deformed grains are small enough to fall below the threshold and are classified as recrystallized. The overall effect of this is considered negligible, as the number of erroneously classified grains will be small. Here we also note that any mDRX occurring during the quench delay will lead to an overestimation of the DRX fraction. Considering the time dependence of DRX from the current data (i.e. the increase in DRX fraction with test duration rather than strain), the increase in DRX fraction with time in the strain range where the process is fastest ($0.2 \leq \varepsilon \leq 0.8$) we estimate an mDRX rate of around 0.07 s^{-1}. The increase in DRX fraction during the 0.2 s quench delay is therefor expected to be less than 0.02 and can be neglected.

The evolution of DRX fraction (black), average recrystallized grain size (blue) and number density of DRX grains (orange) are shown in Fig. 5. Due to low statistics the average grain size has been excluded for strains < 0.2. Up to a strain of 0.8 the primary recrystallization mechanisms seems to be the nucleation of new grains. The number density increases rapidly while the average grain size of recrystallized grains remains rather constant. However this changes for strains over 0.8, as indicated in Fig. 5 where a decrease in the number density and an increase in the average grain size is observed. This result differs from that obtained by Zhang et al. [29] who reported a large increase in DRX grain size, from 6 to 14 μm, between strains 0.3 and 0.5, followed by a relatively constant grain size at larger strains. The tests in [29] were however performed at higher temperature (1110 °C) and strain rates (0.01 s^{-1}), which would be expected to significantly affect the DRX response.

The kinetics of the DRX process can be described by an Avrami-type equation [25,30,31], derived from the corresponding time-dependent expression for static recrystallization [24].

$$X_{DRX} = 1 - \exp\left[-k\left(\frac{\varepsilon - \varepsilon_c}{\varepsilon_p}\right)^n\right]$$

(1)

where X_{DRX} is the recrystallized fraction, ε_c the critical strain for onset of DRX and k and n are strain rate and temperature dependent material constants. Here, we set $\varepsilon_p = 0.15$ according to the stress–strain curves, and $\varepsilon_c = 0.1$ was chosen as an upper bound for the initiation of recrystallization, as the EBSD investigation indicated very limited DRX at this strain. The exact value of ε_c does not have a significant impact on the results. Eq. (1) was then fitted to the values of X_{DRX} determined from EBSD, as the intercept and slope of a linear regression of $\ln(-\ln(1 - X_{DRX}))$ versus $\ln((\varepsilon - \varepsilon_c)/\varepsilon_p)$, to determine the constants $k = 0.1373 \pm 0.016$ and $n = 1.6195 \pm 0.014$, Fig. 6.

Based on post-deformation optical microscopy, Shi et al. [10] reported that DRX of Haynes 282 was not complete after compression to $\varepsilon = 0.7$ at temperatures up to 1120 °C, for a strain rate of 0.1 s^{-1}. At 1050 °C a large fraction of deformed grains remained (although the actual value was not reported), whereas at 1100 and 1120 °C only small unrecrystallized areas remained. After deformation at a slower strain rate, 0.01 s^{-1}, the samples were fully recrystallized at $\varepsilon = 0.7$ at 1100 °C, but the results for lower temperatures were not reported. This qualitatively agrees with our results, but we also note that the quench delay, which can have a significant effect on the recrystallized fraction since mDRX and not DRX will occur during this time, was not reported in [10].
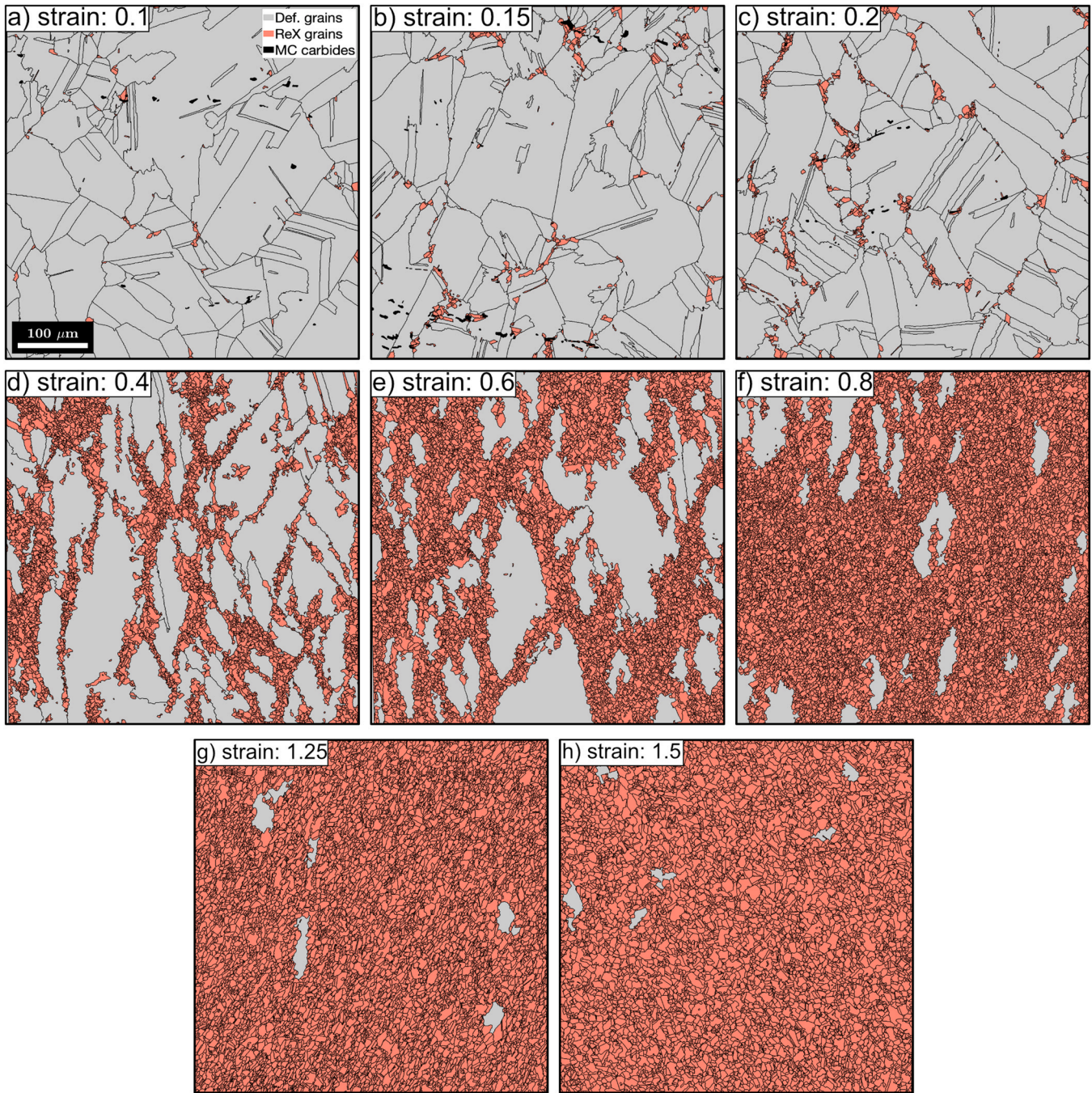
Fig. 4. Maps showing recrystallized grains in red, deformed grains in gray and MC carbides in (a–c) in black. (a) microstructure after a strain of 0.1, (b) 0.15, (c) 0.2 (d) 0.4 (e) 0.6, (f) 0.8, (g) 1.25 and (h) 1.5.

3.5. Estimation of DRX from stress–strain response

Determination of the DRX kinetics from microstructural investigations of interrupted tests is relatively uncommon in the literature, not least due to the considerable amount of testing and evaluation required. Instead, kinetics are often derived from the stress–strain response according to [32].

$$X_{DRX}(\varepsilon) = \frac{\sigma_{DRV}(\varepsilon) - \sigma(\varepsilon)}{\sigma_s - \sigma_{ss}} \qquad (2)$$

where $\sigma_{DRV}(\varepsilon)$ is the stress evolution if no DRX occurs, i.e. by only considering the balance between work hardening and dynamic recovery which saturates at σ_s, and σ_{ss} is the steady state stress, i.e. the stress reached when the work hardening and DRX rates reach

dynamic equilibrium. To compare the two approaches (microstructure evaluation of interrupted tests and determination of X_{DRX} from stress response), we use Eq. (2) to calculate X_{DRX}. The "DRX-free" stress response was described by a Voce-type equation
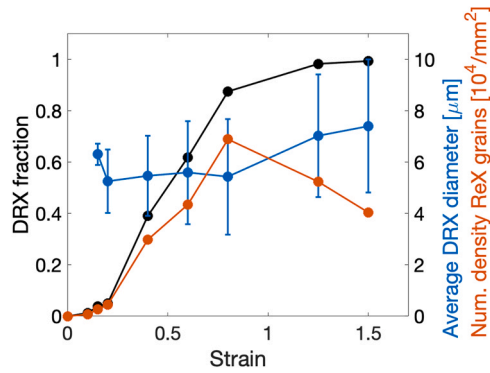
$$\sigma_{DRV}(\varepsilon) = \sigma_s - (\sigma_s - \sigma_0)\exp\{-\alpha\varepsilon\} \qquad (3)$$

where σ_0 is the yield stress and α is a constant. Differentiating Eq. (3) with respect to ε and inserting the inverted form ($\varepsilon = f(\sigma)$) of the same equation leads to the common form
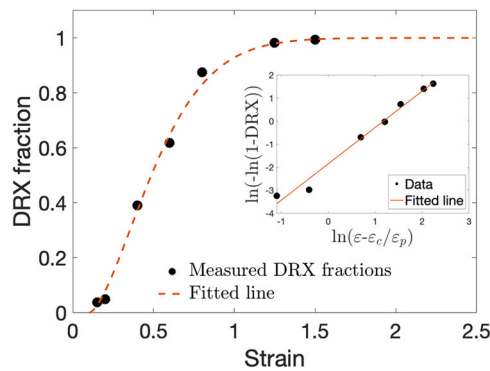
$$\theta = \frac{\partial\sigma_{DRV}}{\partial\varepsilon} = \alpha(\sigma_s - \sigma). \qquad (4)$$

Consequently, α and σ_s can be found from the slope and x-axis intercept of a linear fit of θ vs. σ in the strain range unaffected by

Fig. 5. Evolution of recrystallized fraction (left axis), and average size and number density of recrystallized grains (right axis).

Fig. 6. Fit of an Avrami-type expression (Eq. (1)) to the measured DRX fractions, extrapolated to larger strains to determine the predicted strain levels corresponding to full recrystallization. The linear fit to determine k and n is shown as an insert.

DRX. The steady-state stress σ_{ss} is found from the second intercept of θ with the x-axis. Examples of fitting can be seen in Fig. 7(a) and (b), and the resulting predictions of X_{DRX} for the different samples using Eq. (2) are shown in Fig. 7(c) where they are compared to the experimental values and the Avrami fit (Eq. (1)). The predicted and measured values agree reasonably well, except in the region below $\varepsilon = 0.4$ for the sample deformed to a strain of 0.8. This discrepancy is, however, mainly related to the stress development in the particular sample. Looking closer at the stress–strain curves in Fig. 2(a), we note that a second stress maximum can be observed at $\varepsilon \approx 0.4$ in the sample deformed to a strain of $\varepsilon = 0.8$. This behaviour is not seen in the other samples and is associated with a temperature fluctuation, see Fig. 2(b). All samples with a strain above 0.4 were evaluated using the same approach, except for determination of σ_{ss} which was assumed to be the same for all samples (determined from the sample deformed to $\varepsilon = 1.5$ since the lower maximum strains did not allow reliable extrapolation), and it is clear that the experimental and calculated data agree rather well even at low strains.

In spite of the apparently good agreement between EBSD- and stress-based methods to determine the DRX fraction, there are some caveats, such as the difference in terms of the considered sample volume in the two methods. As noted already, the strain, strain rate and temperature, and consequently the extent of DRX, are not homogeneous in the sample. The recrystallized fraction determined by Eq. (2) depends on the macroscopic stresses and strains, and is strictly only valid in the case of homogeneous DRX in the sample (or at least through the cross-section). In reality, however, the analysis will be the average behaviour of the sample with varying fractions of recrystallized and non-recrystallized regions. Furthermore, the analysis typically excludes the stress-reduction arising from the increased cross-sections due to progressive barrelling of the sample during compression. In the EBSD-based approach, on the other hand, the DRX fractions were obtained from a limited area in the central region of the sample volume, where the strains and temperatures are highest [33,34]. The DRX fractions at the edges and further towards the anvils, and hence the average DRX fraction in the sample, will be significantly lower, and Eq. (1) will therefore overestimate the average DRX fraction in the sample. Notably, the fact that the local strains and temperatures in the central region have been higher than the average corresponding values means that the deformation has locally progressed much further (i.e. the "true" strain points corresponding to the location where the DRX fractions were determined by EBSD should be shifted to the larger strains). This, in turn, suggests that care should be taken when comparing DRX fractions determined from microstructure investigations and stress–strain based calculations.

3.6. Grain boundary evolution

Fig. 8 shows the spatial distribution of different types of grain boundaries in the microstructure. LAGB (< 15°) are shown in blue, random HAGB (≥15°) in black and Σ3 CSL boundaries in red. In Fig. 8(b–d) MC carbides are shown in black, and recrystallized grains in pink. The grains in the billet material (Fig. 8(a)) contains a large number of annealing twins, and no internal substructures. At the lower strains, substructures seen as LAGB in Fig. 8(b–d) progressively develop. These initially accumulate at the pre-existing HAGB, leading to nucleation of recrystallization, most notably in Fig. 8(c) where the two regions with highest density of recrystallized grains also have the largest amount of LAGB substructures surrounding them (marked with black rectangles). In the early stages original Σ3 boundaries appear to be free of surrounding LAGBs. As the deformation progress they lose their coherent structure and become random HAGBs. At a strain of 0.2, Fig. 8(d), there are almost no Σ3 boundaries (red) present. At higher strains, new Σ3 boundaries appear, associated with the recrystallized grains. It has been shown that nuclei can be cut off from their parent by a Σ3 boundary [11], but closer inspection of the maps in Fig. 8 shows that the majority of the Σ3 boundaries are located inside recrystallized grains, suggesting that they are growth twins.

A more statistical representation of the grain boundary distribution evolution is shown in Fig. 9. In Fig. 9(a) the *relative length fractions* of LAGBs and HAGBs are shown as a function of average strain. Note that the closed black symbols show only random HAGBs, whereas the open black symbols represent the sum of random HAGBs (i.e. misorientation angles above 15° but not classified as Σ3) and Σ3 boundaries. The red shaded area between the two thus represents the Σ3 boundaries. Fig. 9(b), on the other hand shows *the total length* of each grain boundary type. The grain boundary evolution is an important aspect as it can help optimize processing parameters in terms of optimal grain boundary structures so called grain boundary engineering [35] where the Σ3 twin boundaries are of particular interest due to their relatively low energy and mobility.
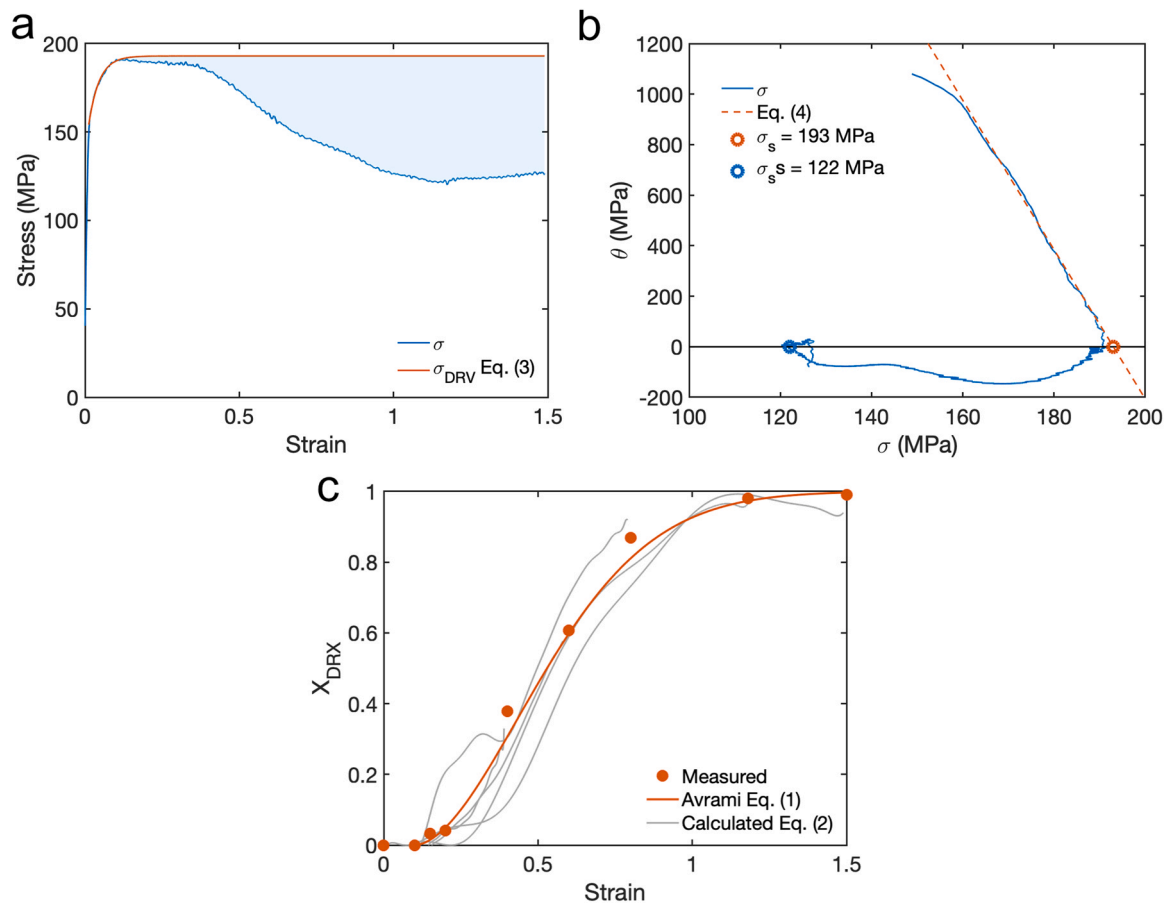
Fig. 7. (a) Stress–strain curve with measured stress strain data of the sample deformed to a strain of 1.5 in blue and σ_{DRV} (Eq. (3)) in orange. (b) Kocks-Mecking plot of the sample deformed to a strain of 1.5 with corresponding σ_s and σ_{ss} marked. (c) shows the measured X_{DRX} values and the fit based on Eq. (1) in orange and the X_{DRX} behaviour with strain based on Eq. (2) for each sample deformed to a strain ≥ 0.4 in gray.

Initially, the majority of HAGB are Σ3, but the length fraction for these decrease significantly between strains 0–0.2. This is caused by the introduction of lattice rotations by the plastic deformation [36]. It is most prevalent between strains 0 and 0.1 where the majority of Σ3 boundaries are transformed into random HAGB, as seen in the large increase in the random HAGB fraction in Fig. 9(a) while the total length for HAGB + Σ3 remains almost constant, Fig. 9(b). The Σ3 fraction and length start to increase at higher strains, due to the creation of growth twins via stacking faults during the motion of HAGB, as well as bulges being cut-off from the parent grain via the creation of a twin boundary [37]. With nucleation of new grains one can see an increase in the total Σ3 length suggesting that twinning is a part of the dDRX process, which has been reported by other authors as well [38,39]. However, the results from Azarbarmas et al. [39] suggests that the twinning process is highly temperature-dependent, as a significantly lower amount of Σ3 boundaries were created during deformation of Inconel 718 at 1000 °C compared to at 1050 °C.

An increasing plastic deformation initially leads to a gradual increase in the LAGB length as dislocation structures build up in the grain interiors. The amount of HAGB (random + Σ3), on the other hand, increases very slowly in the early stages, which leads to an increase in the fraction of LAGBs up to a strain of 0.2, after which it

decreases again. This decrease is not a result of a decreasing density of LAGBs. This is seen by the continuing increase in the LAGB length up to a strain of 0.4, and can also be qualitatively seen in Fig. 8. At strains above 0.2, more and more HAGBs are introduced by the DRX process, which is the reason for the decreasing LAGB fraction in spite of the still increasing LAGB length. Starting from $\varepsilon = 0.8$, also the LAGB length (not only the fraction) starts to decrease. This is likely a combined effect of the decreasing fraction of deformed grains (increasing DRX fraction), leading to a smaller area containing LAGBs, and accelerated dynamic recovery which reduces the LAGB density. The latter can be qualitatively seen by comparing Fig. 8(e) and (f), where the density of LAGBs in the large deformed grains is clearly lower at a strain of 0.6 (f) compared to 0.4 (e).

3.7. Substructures in DRX grains

Another observation was that even at lower strains internal structures existed in small, recrystallized, grains. Examples of this is shown in Fig. 10, where magnified views of samples deformed to $\varepsilon = 0.1$ (a), 0.15 (b) and 0.2 (c), are shown. The arrows highlight small grains of similar size, where red arrows point to grains *without* internal structures, while black arrows indicate grains *with* internal structures. This contradicts the general notion that DRX grains are
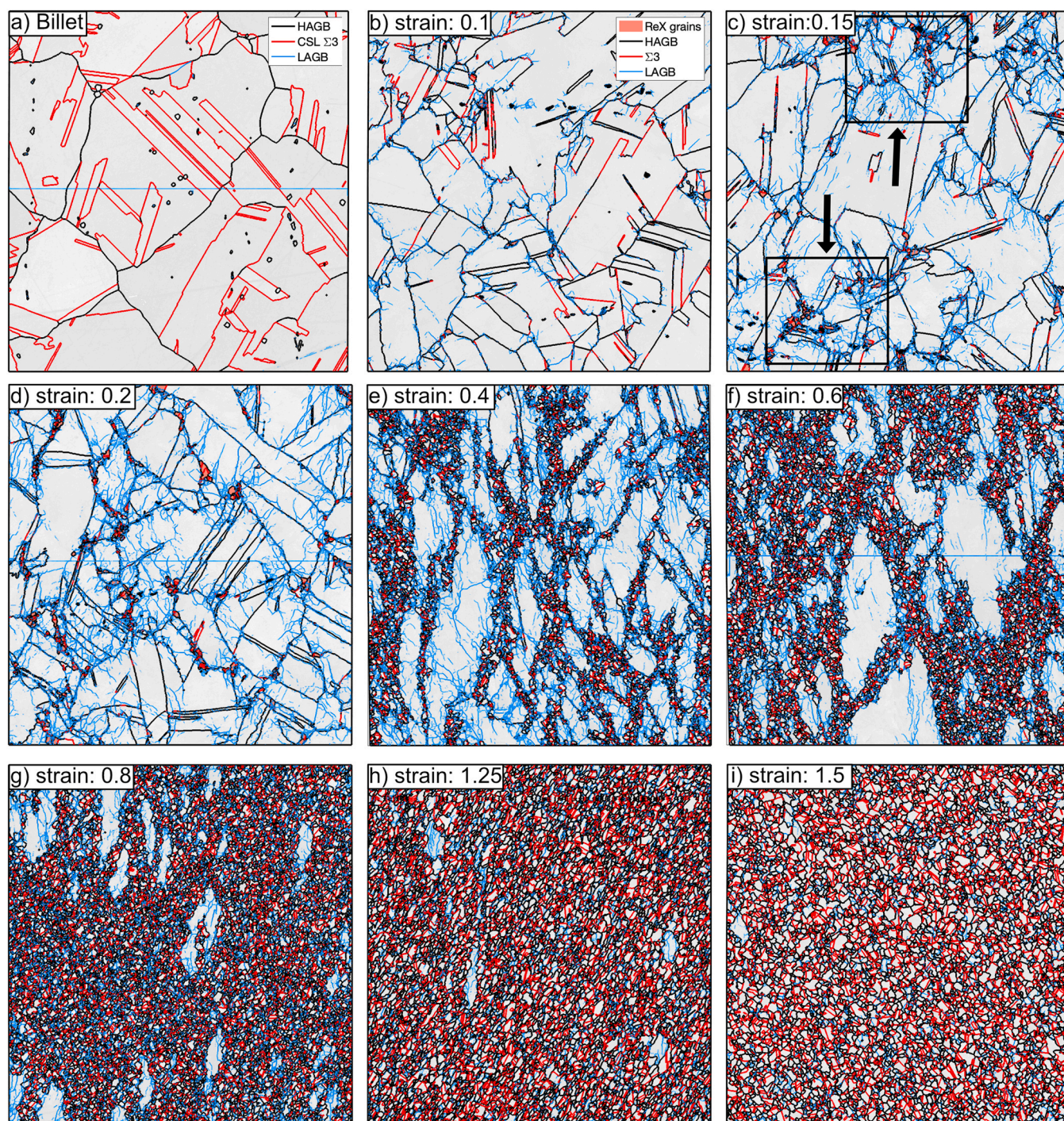
Fig. 8. Grain boundaries in the billet (a) and after compression to different strains (b–i). LAGBs (< 15°) are shown blue, random HAGBs in black and Σ3 CSL boundaries in red. In the samples were MC carbides were manually removed (b–d) carbides are marked in black and recrystallized grains in pink. Blue horizontal lines in the middle of (a), (d) and (f) originate from imperfect stitching of the two partial maps. Black rectangles in (c) highlight a higher concentration of LAGB and regions of recrystallized grains.

initially deformation free. Even though recrystallized grains do become progressively deformed with continued compression, it seems unlikely that such pronounced substructures would have had time to develop for these low strains. In order to exclude the possibility of artefacts from grinding and polishing one sample was instead ion etched in a Gatan precision etching coating system (PECS) in order to remove possible deformation of the surface. However, small grains with apparent substructures were still present. In order to draw any further conclusions, a dedicated analysis using transmission electron microscopy (TEM) is required.
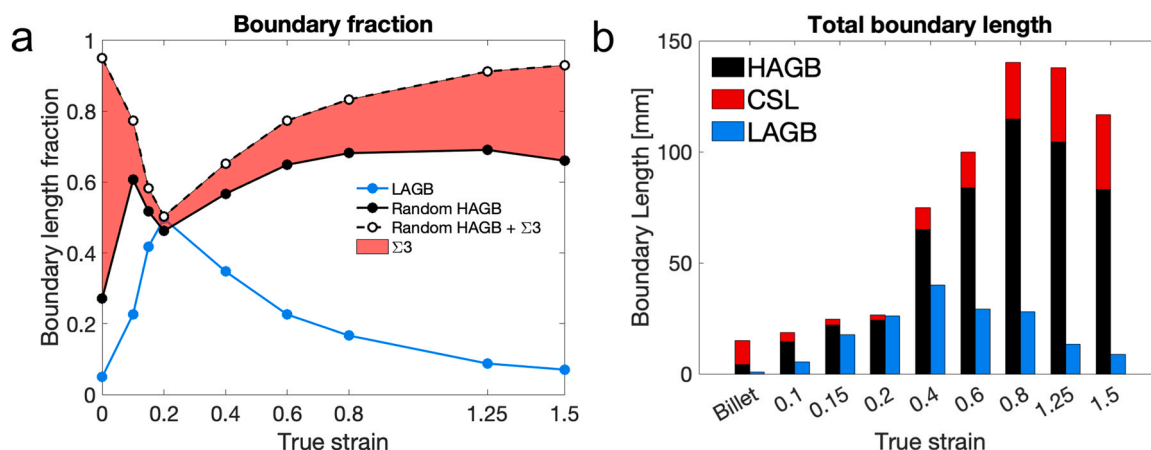
Fig. 9. Grain boundary misorientation statistics. (a) Length fractions for LAGBs (< 15°) in blue, random HAGB (> 15°, excluding Σ3 boundaries) in solid black closed circles and random HAGB + Σ3 twin boundaries in dashed black open circles. The red shaded area shows the Σ3 fraction. (b) Total length of LAGBs (blue), random HAGBs (black) and Σ3 boundaries (red).
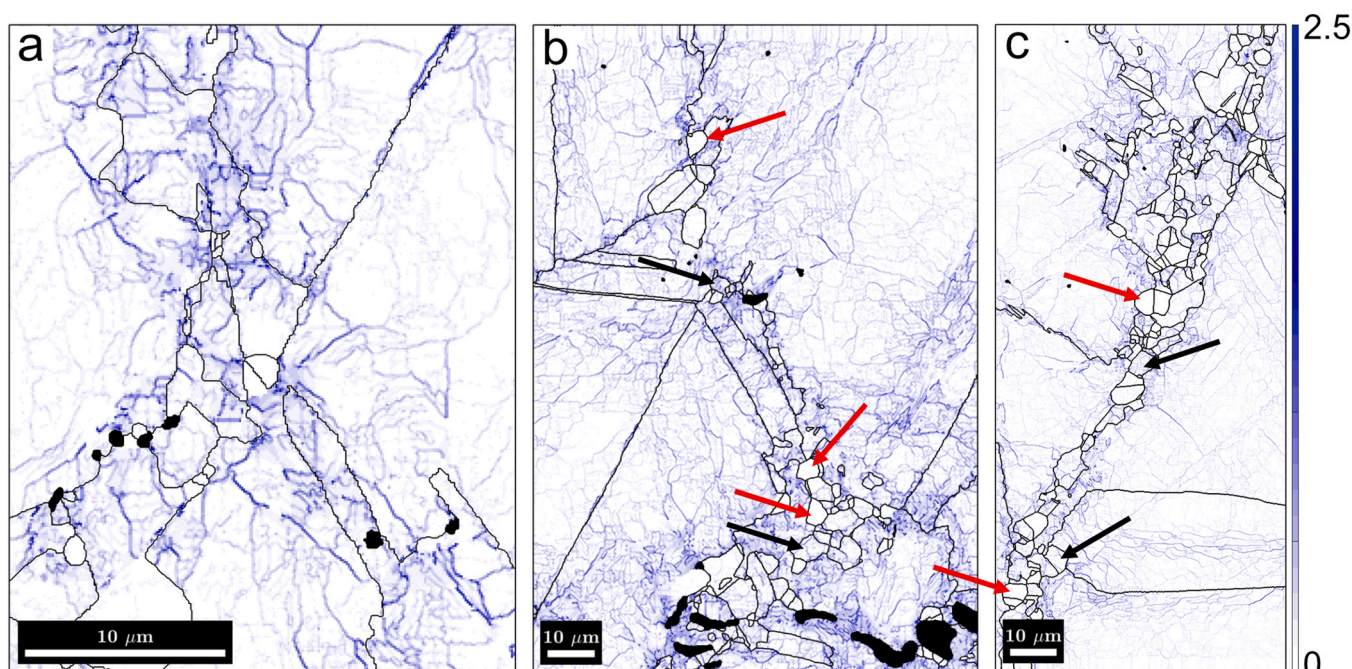
Fig. 10. KAM maps of magnified regions in the maps in Fig. 3 for (a) $\varepsilon = 0.1$, (b) $\varepsilon = 0.15$ and (c) $\varepsilon = 0.2$. Note that the scale for the KAM maps are 0–2.5°, so local misorientations above this value will not be seen. MC carbides are marked in black. Black arrows points at small grains with substructures, while red arrows point to grains with similar size without internal structures. Scale bars are 10 μm.

4. Conclusion

- During deformation of Haynes 282 compressed at a strain rate of 0.05 s^{-1} at 1080 °C individual DRX grains could be observed already at $\varepsilon = 0.1$, i.e. before the peak strain $\varepsilon_p = 0.15$.
- The DRX process accelerated significantly above $\varepsilon = 0.2$, and the material was fully recrystallized at $\varepsilon = 1.5$.
- Continuous nucleation of new grains, rather than growth of early recrystallized grains, occurs during deformation up to a strain of $\varepsilon = 0.8$ which results in an increase in the fraction and total length of Σ3 boundaries with increasing strain.
- At higher strains the increase in DRX fraction is caused by grain growth. The kinetics are well described by an Avrami-type equation, and can be predicted from the stress evolution with good accuracy.
- Many small grains classified as recrystallized still contained distinct deformation substructures, even at very low strains, contrary to the conventional notion of DRX grains being deformation free.

Declaration of Competing Interest

The authors declare that they have no known competing financial interests or personal relationships that could have appeared to influence the work reported in this paper.

Acknowledgements

Appendix A. Supporting information

Supplementary data associated with this article can be found in the online version at doi:10.1016/j.jallcom.2023.170837.

References

[1] C. Cui, Y. Gu, Y. Yuan, T. Osada, H. Harada, Enhanced mechanical properties in a new Ni-Co base superalloy by controlling microstructures, Mater. Sci. Eng.: A 528 (16–17) (2011) 5465–5469, https://doi.org/10.1016/j.msea.2011.03.085

[2] M.J. Donachie, S.J. Donachie, Superalloys: A Technical Guide, A S M International, Materials Park, UNITED STATES, 2002.

[3] R.C. Reed, The Superalloys: Fundamentals and Applications, Cambridge University Press, Cambridge, UNITED KINGDOM, 2006.

[4] L. Pike, Development of a Fabricable Gamma Prime Strengthened Superalloy, In: Superalloys 2008 (Eleventh International Symposium), TMS, 2008, 191–200.10. 7449/2008/Superalloys2008191200.

[5] K. Kruger, HAYNES 282 alloy, Materials for ultra-supercritical and advanced ultra-supercritical power plants, Elsevier, 2017, pp. 511–545, https://doi.org/10. 1016/B978-0-08-100552-1.00015-4

[6] C. Joseph, C. Persson, M.H. Colliander, Influence of heat treatment on the microstructure and tensile properties of Ni-base superalloy Haynes 282, Mater. Sci. Eng.: A 679 (2017) 520–530, https://doi.org/10.1016/j.msea.2016.10.048

[7] N.R. Jaladurgam, H. Li, J. Kelleher, C. Persson, A. Steuwer, M.H. Colliander, Microstructure-dependent deformation behaviour of a low γ? volume fraction Ni-base superalloy studied by in-situ neutron diffraction, Acta Mater. 183 (2020) 182–195, https://doi.org/10.1016/j.actamat.2019.11.003

[8] S. Mukherjee, K. Barat, S. Sivaprasad, S. Tarafder, S.K. Kar, Elevated temperature low cycle fatigue behaviour of Haynes 282 and its correlation with microstructure - effect of ageing conditions, Mater. Sci. Eng.: A 762 (2019) 138073, , https://doi.org/10.1016/j.msea.2019.138073

[9] K.-Y. Shin, J.-H. Kim, M. Terner, B.-O. Kong, H.-U. Hong, Effects of heat treatment on the microstructure evolution and the high-temperature tensile properties of Haynes 282 superalloy, Mater. Sci. Eng.: A 751 (2019) 311–322, https://doi.org/10.1016/j.msea.2019.02.054

[10] Z. Shi, X. Yan, C. Duan, C. Tang, E. Pu, Characterization of the hot deformation behavior of a newly developed nickel-based superalloy, J. Mater. Eng. Perform. 27 (2018) 1763–1776, https://doi.org/10.1007/s11665-018-3270-5

[11] E. Eriksson, M. HörnqvistColliander, Dynamic and post-dynamic recrystallization of haynes 282 below the secondary carbide solvus, Metals 11 (2021) 122, https://doi.org/10.3390/met11010122

[12] D. Metzler, M.G. Fahrmann, The Effect of Prior TMP on Annealed Grain Size in HAYNES 282 Alloy, In: 8th International Symposium on Superalloy 718 and Derivatives(2014)379–389.10.1002/9781119016854.ch30.

[13] E. Eriksson, J. Andersson, M. Hörnqvist Colliander, The effect of grain boundary carbides on dynamic recrystallization during hot compression of ni-based superalloy haynes 282, Metall. Mater. Trans. A 53 (2022) 29–38, https://doi.org/10.1007/s11661-021-06524-x

[14] S. Gardner, W. Li, M. Coleman, R. Johnston, The effects of thermomechanical history on the microstructure of a nickel-base superalloy during forging, Mater. Sci. Eng.: A 668 (2016) 263–270, https://doi.org/10.1016/j.msea.2016.05.051

[15] S.S. SatheeshKumar, T. Raghu, P.P. Bhattacharjee, G. AppaRao, U. Borah, Constitutive modeling for predicting peak stress characteristics during hot deformation of hot isostatically processed nickel-base superalloy, J. Mater. Sci. 50 (2015) 6444–6456, https://doi.org/10.1007/s10853-015-9200-0

[16] E. Poliak, J. Jonas, A one-parameter approach to determining the critical conditions for the initiation of dynamic recrystallization, Acta Mater. 44 (1996) 127–136, https://doi.org/10.1016/1359-6454(95)00146-7

[17] A. Nicolaÿ, G. Fiorucci, J. Franchet, J. Cormier, N. Bozzolo, Influence of strain rate on subsolvus dynamic and post-dynamic recrystallization kinetics of Inconel 718, Acta Mater. 174 (2019) 406–417, https://doi.org/10.1016/j.actamat.2019.05.061

[18] A. Amiri, S. Bruschi, M.H. Sadeghi, P. Bariani, Investigation on hot deformation behavior of Waspaloy, Mater. Sci. Eng.: A 562 (2013) 77–82, https://doi.org/10.1016/j.msea.2012.11.024

[19] A. Nicolaÿ, J.M. Franchet, J. Cormier, R.E. Logé, G. Fiorucci, J. Fausty, M. Van Der Meer, N. Bozzolo, Influence of joule effect heating on recrystallization phenomena in inconel 718, Metall. Mater. Trans. A 52 (2021) 4572–4596, https://doi.org/10.1007/s11661-021-06411-5

[20] M.G. Fahrmann, L.M. Pike, Experimental TTT Diagram of HAYNES 282 Alloy, In: 9th International Symposium on Superalloy 718 and Derivatives(2018)565–578. 10.1007/978–3-319–89480-5_37.

[21] C. Joseph, M. Thuvander, C. Persson, M. Hörnqvist Colliander, Precipitation of γ' during cooling of nickel-base superalloy Haynes 282, Philos. Mag. Lett. 101 (2021) 30–39, https://doi.org/10.1080/09500839.2020.1841314

[22] G. Nolze, R. Hielscher, Orientations - perfectly colored, J. Appl. Crystallogr. 49 (2016) 1786–1802, https://doi.org/10.1107/S1600576716012942

[23] C. Joseph, C. Persson, M. HörnqvistColliander, Precipitation kinetics and morphology of grain boundary carbides in Ni-BASE SUPERALLOY HAYnes 282, Metall. Mater. Trans. A 51 (2020) 6136–6141, https://doi.org/10.1007/s11661-020-06019-1

[24] J.J. Jonas, X. Quelennec, L. Jiang, É. Martin, The Avrami kinetics of dynamic recrystallization, Acta Mater. 57 (2009) 2748–2756, https://doi.org/10.1016/j.actamat.2009.02.033

[25] X.M. Chen, Y.C. Lin, D.X. Wen, J.L. Zhang, M. He, Dynamic recrystallization behavior of a typical nickel-based superalloy during hot deformation, Mater. Des. 57 (2014) 568–577, https://doi.org/10.1016/j.matdes.2013.12.072

[26] J. McCarley, R. Helmink, R. Goetz, S. Tin, Grain boundary engineering of a low stacking fault energy Ni-based superalloy, Metall. Mater. Trans. A 48 (2017) 1666–1677, https://doi.org/10.1007/s11661-017-3977-1

[27] H. Miura, T. Sakai, H. Hamaji, J. Jonas, Preferential nucleation of dynamic recrystallization at triple junctions, Scr. Mater. (2004) 65–69, https://doi.org/10.1016/j.scriptamat.2003.09.035

[28] E. Eriksson, Dynamic and meta-dynamic recrystallization of Ni-based superalloy Haynes 282, Ph.D. thesis, Chalmers University of Technology (2022).

[29] H. Zhang, S. Qin, H. Li, J. Liu, Y. Lv, Y. Wang, P. Zhang, H. Zhou, T. Wu, EBSD study of strain dependent microstructure evolution during hot deformation of a typical nickel-based superalloy, J. Mater. Res. 34 (2019) 321–334, https://doi.org/10.1557/jmr.2018.393

[30] L. Wang, F. Liu, Q. Zuo, C. Chen, Prediction of flow stress for N08028 alloy under hot working conditions, Mater. Des. 47 (2013) 737–745, https://doi.org/10.1016/j.matdes.2012.12.074

[31] D. Liu, H. Chai, L. Yang, W. Qiu, Z. Guo, Z. Wang, Study on the dynamic recrystallization mechanisms of GH5188 superalloy during hot compression deformation, J. Alloy. Compd. 895 (2022) 162565, , https://doi.org/10.1016/j.jallcom.2021.162565

[32] A. Laasraoui, J.J. Jonas, Prediction of steel flow stresses at high temperatures and strain rates, Metall. Trans. A 22 (1991) 1545–1558, https://doi.org/10.1007/BF02667368

[33] R. Buckingham, C. Argyrakis, M. Hardy, S. Birosca, The effect of strain distribution on microstructural developments during forging in a newly developed nickel base superalloy, Mater. Sci. Eng.: A 654 (2016) 317–328, https://doi.org/10.1016/j.msea.2015.12.042

[34] N. D'Souza, W. Li, C. Argyrakis, G.D. West, C.D. Slater, On the evolution of primary gamma prime precipitates during high temperature and high strain rate deformation and subsequent heat treatment in the Ni-based superalloy, RR1000, Metall. Mater. Trans. A 50 (2019) 4205–4222, https://doi.org/10.1007/s11661-019-05330-w

[35] N. Souaï, N. Bozzolo, L. Nazé, Y. Chastel, R. Logé, About the possibility of grain boundary engineering via hot-working in a nickel-base superalloy, Scr. Mater. 62 (2010) 851–854, https://doi.org/10.1016/j.scriptamat.2010.02.019

[36] H. Zhang, K. Zhang, S. Jiang, H. Zhou, C. Zhao, X. Yang, Dynamic recrystallization behavior of a gamma prime-hardened nickel-based superalloy during hot deformation, J. Alloy. Compd. 623 (2015) 374–385, https://doi.org/10.1016/j.jallcom.2014.11.056

[37] K. Huang, R.E. Logé, A review of dynamic recrystallization phenomena in metallic materials, Mater. Des. 111 (2016) 548–574, https://doi.org/10.1016/j.matdes.2016.09.012

[38] H. Zhang, H. Zhou, S. Qin, J. Liu, X. Xu, Effect of deformation parameters on twinning evolution during hot deformation in a typical nickel-based superalloy, Mater. Sci. Eng.: A 696 (2017) 290–298, https://doi.org/10.1016/j.msea.2017.04.077

[39] M. Azarbarmas, M. Aghaie-Khafri, J. Cabrera, J. Calvo, Dynamic recrystallization mechanisms and twining evolution during hot deformation of Inconel 718, Mater. Sci. Eng.: A 678 (2016) 137–152, https://doi.org/10.1016/j.msea.2016.09.100